Free Standing Nanoporous Pd Alloys as CO Poisoning Tolerant Electrocatalysts for the Electrochemical Reduction of CO₂ to Formate

Swarnendu Chatterjee^a, Charles Griego^b, James L. Hart^c, Yawei Li^a, Mitra L. Taheri^c, John Keith^b, and Joshua D. Snyder^{a*}

a Department of Chemical and Biological Engineering, Drexel University, 3141 Chestnut Street, Philadelphia, Pennsylvania 19104, United States

b Department of Chemical and Petroleum Engineering, University of Pittsburgh, 3700 O'Hara Street, Pittsburgh, PA 15261

c Department of Materials Science and Engineering, Drexel University, 3141 Chestnut Street, Philadelphia, Pennsylvania 19104, United States

* Corresponding author: jds43@drexel.edu

Abstract

CO₂ electrochemical reduction to formate has emerged as one of the promising routes for CO₂ conversion to useful chemicals and energy storage. Palladium has been shown to make formate with a high selectivity at minimal overpotential. However, production of CO as a minor product quickly deactivates the catalyst during extended electrolysis. Here, we present nanoporous Pd alloys (np-PdX) formed by electrochemical dealloying of Pd₁₅X₈₅ alloys (X = Co, Ni, Cu, and Ag) as active free standing electrocatalysts with high formate selectivity and CO poisoning tolerance. Rate of deactivation under constant potential electrolysis, due to CO passivation, is strongly correlated to the identity of the transition metal alloying component. We purport that this composition dependent behavior is due to the induced electronic changes in the active Pd surface, affecting both the CO adsorption strength and the near surface hydrogen solubility which can

impact the adsorption strength of active/inactive intermediates and reaction selectivity. Free-standing np-PdCo and np-PdNi are found to exhibit high areal formate partial current densities, > 20 mA cm⁻², with high CO poisoning tolerance and minimal active area loss at cathodic potentials, demonstrating the utility of these materials for selective and stable CO₂ electrolysis.

Keywords: Carbon dioxide reduction, electrocatalysis, nanoporous metals, electrolysis, dealloying

1. Introduction

The capture and sequestration of atmospheric CO₂ has become one of the great challenges of our society as its rate of production and accumulation scales with population growth. Aqueous phase electrochemical reduction of CO₂ (CO₂RR) to hydrocarbon fuels, value added chemicals, and chemical precursors/feedstock shows great promise for both anthropogenic CO₂ remediation and on-demand storage of energy generated from renewable sources such as solar and wind¹⁻³. There are, however, three critical limitations that must be addressed to further advance the potential commercial integration of CO₂ electrolysis: (1) high overpotential⁴⁻⁸, (2) poor selectivity ^{4,6-11}, and (3) low aqueous phase solubility of CO₂¹². The high stability of the nonpolar CO₂ molecule and the multiple proton/electron transfer steps required to produce the desired reduced products present a great technological challenge to the development of next generation electrocatalytic materials. CO₂RR rate and selectivity are sensitive to the general material properties of the catalyst (conductivity, reactant/intermediate/product adsorption free energy, etc.), applied overpotential, near surface pH, etc.¹³. This gives rise to a varied range of products including CO, formate/formic acid, H₂, alcohols, and hydrocarbons ranging from C1 to multiple carbon species. Consequently, overall selectivity for one single product is low^{11,14–16}.

CO₂RR active transition metals are grouped according to the reduced products that they are capable of forming^{6-9,17-21}. Metals with low hydrogen overpotentials and strong CO binding, Pt, mostly produce H₂ and CO in aqueous media^{8,17}. Moderate CO binding metals such as Ag and Au produce CO almost exclusively $^{20-23}$. Cu is the only transition metal that is capable of producing a broad range of hydrocarbons with any appreciable faradaic efficiency (FE)⁷⁻⁹. Weak CO binding metals with high hydrogen overpotentials such as Hg, Cd, Pb, Tl, In, Bi, and Sn typically reduce CO₂ to HCOO-/HCOOH (formate/formic acid), dependent upon electrolyte pH, with high selectivity but at overpotentials approaching 1 V^{6,8,9,17–19,24–26}. In contrast to the production of alcohols and hydrocarbons, the 2-e⁻ reduction of CO₂ to CO and HCOO⁻/HCOOH can be accomplished with high selectivity on a range of materials^{6,8,24–26,9,17–23}. The minimal number of concerted proton/electron transfers limits the product distribution for CO₂RR with H₂ likely being the only side product. This presents a distinct advantage over process development for the reduction of CO₂ to more reduced products including alcohols and hydrocarbons. HCOO-/HCOOH has great utility as both an electrochemical fuel^{27–31} and a chemical precursor^{32–35}, making it a more desirable reduced product than CO. The high overpotentials, as large as 1 V in some cases^{6,8,9,17–19,24–26}, on traditional HCOO-/HCOOH evolving metals, however, is a significantly limiting barrier.

In the early surveys of the activity and selectivity of a range of polycrystalline transition metals, Pd, which like Pt is a strong CO binding metal, was found to evolve CO and H₂ as the major products³⁶. More recent work by Kanan³⁷ and Koper¹⁸ have demonstrated that at low overpotentials, < ~200 mV, Pd nearly exclusively reduces CO₂ to HCOO⁻/HCOOH with FEs approaching 100% at geometric current densities as high as 6.5 mA cm⁻² ^{18,37}. Increasing the overpotential beyond ~ 500 mV changes the selectivity to H₂/CO with their molar ratios being a

function of overpotential³⁸. The 2-electron CO₂RR to HCOO (near neutral bicarbonate electrolytes), with a reversible potential of approximately 0.02 V vs. RHE³⁹ has been termed an electrohydrogenation process where the simultaneous transfer of a proton and electron forms an adsorbed HCOO_{ad} intermediate rather than CO_{ad}³⁷. The source of the high electrohydrogenation activity of Pd has been suggested to be due to its ability to form a saturated hydride phase near 0 V vs. RHE⁴⁰⁻⁴², H/Pd ratios as high as 0.7^{43} . The difference in observed FE and selectivity for HCOO when comparing planar, polycrystalline electrodes to nanostructured materials is likely related to the rate of formation and degree/ease of participation of the α , β -PdH active phase, which is likely more facile on nanostructured surfaces with a higher defect density^{37,41,44,45}. The hydride mediated reduction to HCOO HCOOH has also been observed on non-Pd hydrides⁴⁶. The key to the selectivity of Pd is the ability of Pd to form an active hydride phase, shifting to an HCOO_{ad} intermediate rather than a COOH_{ad} intermediate which is the first electron transfer step toward CO_{ad}^{37,41}.

A major limitation of Pd for CO₂ electrolysis is the gradual current decay initiated by the formation of a poisoning CO adlayer³⁷. While the HCOO'/HCOOH FE on Pd at low overpotential is near 100%, slow but consequential rates of the 2-electron CO pathway (< 0.1% FE)³⁷ result in eventual deactivation. This process has received attention recently with groups focusing on the CO tolerance of Pd nanomaterials during CO₂RR electrolysis. Sargent et al.⁴⁷ demonstrated that CO poisoning is suppressed on branched Pd nanoparticles that are composed of high index facets in comparison to other shape controlled particles that are bound by lower index facets. A similar shift to stable electrolysis through CO tolerance at moderate formate FEs was observed for porous Pd structures formed through electrodeposition⁴⁵. The observed operational stability is again likely due to the high index configuration of the tortuous, porous structure. Another strategy involves a

barrier Cu film on the surface of the Pd particles, demonstrating operational longevity during extended electrolysis while still exhibiting a high formate FE⁴⁸. The presence of the underlying Pd weakens the degree of interaction between CO and Cu and limiting the thickness of the Cu film to 1 ML results in a similar product distribution to pure Pd⁴⁸. For CO₂RR, two classes of Pd alloys have been explored: (1) segregated alloys where Pd is the active surface metal⁴⁹ and (2) bimetallic surfaces where there is a cooperative effect between two dissimilar metals on the surface. The first class of Pd alloys including PdCu^{50,51}, PdNi⁵², PdTe⁵³ have mostly been explored for improvement in the rate and selectivity of CO production. Yuhan et al.⁵⁴ have explored the second class of Pd alloys in which a mixed Pd-Sn surface is shown to promote high formate FEs at potentials as low as -0.26 V vs. RHE. More recently, Cai et al.⁵⁵ have extended the operational potential window for high FE formate production on Pd to higher overpotentials, yielding high formate production rates, by doping Pd with 7 at. % boron. They achieved a peak formate FE of 70 % at -0.5 V vs. RHE. Despite these efforts, CO poisoning for CO₂RR within 0.5 V overpotential is still a major challenge for any Pd based catalyst.

Here we present the development of free-standing, nanoporous Pd-X (np-PdX) alloys (X = Ni, Co, Ag, Cu) with high HCOO⁻ FE at low overpotentials and CO poisoning tolerance during extended CO₂RR electrolysis compared to existing Pd/C electrocatalysts. Dealloying of Pd_{0.15}X_{0.85} alloys results in the formation of a Pd-skinned, core-shell bicontinuous nanoporous architecture where the interior of the ligaments retain a high fraction of the X alloying component and the surface is passivated in Pd. We argue that it is the core-shell structure that results in the modification of both the electronic properties of the surface and H-solubility of the bulk solid, changing the degree of interaction with CO and mitigating poisoning. Rate of catalyst deactivation is found to be a result of the combination of alloy composition dependent CO binding strength and

CO adsorption induced hydride capacity shifts. The presented freestanding np-PdX electrodes have advantages over Pd/C including morphological stability, negation of the need for ionomer binders in the catalyst layer, and CO poisoning tolerance during extended CO₂RR electrolysis. With this electrocatalyst architecture we have attained sustainable production of HCOO⁻, which is a highly desirable electrochemical fuel and chemical precursor, at low overpotential with industrially relevant selectivity, current density, and operational durability, both in terms of morphology retention and intermediate poisoning mitigation.

2. Experimental Methods

2.1. Catalyst Synthesis

Pd/C (30 wt.% Pd): Palladium nanoparticles are prepared through organic phase solvothermal reduction⁵⁶. Under N₂ flow, 75 mg Pd(acac)₂ (Palladium (II) acetylacetonate, Sigma Aldrich, assay: 99%) is dissolved in 15 mL of OAm (Oleylamine, Sigma Aldrich, assay: 70%) at 60° C. A separate solution of 300 mg BTB (Borane tert-butylamine complex, Sigma Aldrich, assay: 97%) in 3 – 4 ml OAm is quickly injected into the OAm solution at 60° C. The temperature is increased to 90° C at 3° C/min and kept under stirring for 1 hour. The solution is then cooled to room temperature and mixed with 10 – 20 ml chloroform for uniform dispersion of particles. The cooled solution is added drop wise to a separate solution of 60 mg carbon (Vulcan XC-72R, Fuel cell store) in 200 mL chloroform under sonication. The final mixture is sonicated for 30 minutes. Following loading of the catalyst on the carbon support, 20 mL ethanol is added to precipitate the catalyst under centrifugation (8000 rpm, 20 minutes). Cleaning/collection cycles in hexane/ethanol mixtures are repeated at least three times. After the final cleaning, the collected particles are dried and the resulting Pd/C powder is annealed for 1 hour at 150° C in air to remove residual surfactant

and 2 hours at 250° C in H₂/Ar before use. Electrodes incorporating the Pd/C catalyst are prepared through drop casting of Pd/C ink on Ti flags (1.4 cm x 1 cm, 0.127 mm thick, Alfa Aesar). Ti flags are pre-cleaned in boiling oxalic acid (10% w/v, Alfa Aesar) for 1 hour. The catalyst ink is composed of 2 mg mL⁻¹ Pd/C in isopropanol (2-propanol, Sigma Aldrich, assay: 99.999%). Nafion solution (Ion Power) is added to the ink in an amount that yields a dried catalyst layer with 0.01 wt.% Nafion. Formation of the catalyst layer is accomplished through drop casting of 200 μL of the catalyst ink onto a Ti flag followed by drying under vacuum.

Nanoporous palladium (np-PdX) is prepared by the electrochemical dealloying of $Pd_{15}X_{85}$ (X = Co, Ni, Cu, Ag) alloy foils. Following melting and homogenization of the alloys from high purity precursor metals (Kurt J Lesker, purity above 99.9%) in a radio frequency induction furnace (Ambrell EasyHeat 3542 LI) under Ar, the alloys are rolled into thin ribbons using a rolling mill. Intermittent annealing under Ar is used during the rolling process to remove work hardening and promote homogenization of the precursor alloys. Electrodes are fabricated from the alloy foils by spot welding a \sim 0.25 cm² foil to a Ti wire which was subsequently sealed in epoxy, only exposing one face of the alloy foil.

As a consequence of the strong composition dependence of dealloying rates, dealloying conditions were optimized for each of the different alloys with the goal of attaining similar length scales (pore/ligament size) and residual composition. np-PdCo and np-PdNi are prepared by electrochemical dealloying (three electrode cell with Toray carbon paper counter electrode and Ag/AgCl reference electrode) in Ar purged 10 mM HCl + 0.5 M H₂SO₄ with potential cycling between -0.13 V and 1.02 V vs. RHE 50 mV s⁻¹ (18 cycles). np-PdCu and np-PdAg are prepared by dealloying in 0.1 M H₂SO₄ with potential cycling between 0.47 V and 1.27 V vs. RHE (12 cycles) and in 0.1 M HNO₃ between 0.87 V and 1.52 V (12 cycles), respectively.

2.2. Material Characterization

The structure and surface morphology of Pd/C and np-PdX are analyzed using Transmission Electron Microscopy (TEM) (JEOL JEM2100), Scanning TEM (STEM) electron energy loss spectroscopy (EELS) (JOEL 2100F with a Quantum Gatan Imaging Filter), and Scanning Electron Microscopy (SEM) (Zeiss Supra 50VP). EELS elemental mapping of np-PdX shows the elemental distribution in the ligamentous structure. XPS measurements were performed with a PHI Veraprobe 5000 instrument equipped with Monochromated AlK alpha source. Analysis is made with X-ray settings of 100 micrometer, 25 W e-beam and photoelectrons are collected using hemispherical analyzer. Pass energy is 117 V for surveys. Dual beam neutralization is performed to compensate for depletion of photoelectrons from the surfaces.

2.3. Electrochemical Measurements

All the electrochemical experiments are conducted in a three-electrode electrochemical cell using an Autolab PGSTAT128N potentiostat. The CO₂RR is performed in 1 M KHCO₃ (Sigma Aldrich, 99.7%) made with Millipore water (Milli-Q Synthesis A10). Prior to all experiments, the electrolyte is first purged with Ar followed by CO₂ until saturation, ~30 min. The 1 M KHCO₃ has a pH of 8.4 when Ar purged and a pH of 7.8 when saturated with CO₂. All the experiments involving CO₂RR, polarization curves and extended electrolysis, are performed in a custom-made two compartment gas tight glass cell separated by a Nafion membrane (Ion Power). Electrolysis experiments were run in a semi-batch mode where CO₂ was continually bubbled into the catholyte to ensure continuous saturation, drive electrolyte mixing, and prevent any pH gradients from forming. After extended electrolysis, the catholyte is collected for product analysis. A Ag/AgCl electrode (BASi) is used as the reference electrode with Pt mesh as the counter electrode. All the

glassware is cleaned in a 1:1 v:v solution of concentrated sulfuric and nitric acid followed by boiling in Millipore water before each use.

As Pd and its alloys can absorb hydrogen, CO stripping is used to calculate the electrochemically active surface area of the np-PdX electrodes. A monolayer of CO is deposited onto the np-PdX electrodes by holding the potential at 0.05 V vs. RHE in 0.1 M HClO₄ while bubbling CO into the solution. Following passivation of the surface with CO, the electrolyte is purged with Ar for 30 minutes. The potential is then sweep anodically at a rate of 50 mV/s to oxidize the monolayer of CO. Integration of the CV curves yields the charge associated with CO oxidation which can be converted to ECSA using the conversion factor 420 μC/cm². Roughness factor (RF) is calculated by dividing the ECSA by the geometric area of the electrode.

2.4. Product Quantification

Quantification of HCOO⁻ in the 1 M KHCO₃ electrolyte after constant potential electrolysis is accomplished using a 300 MHz Varian Unity Inova NMR. A minimum of 1 hour of electrolysis is used to build up HCOO⁻ for detection. For the samples that quickly deactivate, electrodes are periodically reactivated³⁷ to continue electrolysis. A sample of the electrolyte post-CO₂RR is mixed (5:1) with a solution of DMSO (Dimethyl Sulfoxide, Sigma Aldrich, 99.9%) and D₂O (7.5 µl DMSO in 15 ml D₂O (Deuterium Oxide, Sigma Aldrich, 99.9%)) which serves as an internal standard. The ¹H spectrum of HCOO⁻ is measured after a pre-saturation protocol.

The faradaic efficiencies (FE) of HCOO⁻ evolution are calculated using the following equation:

$$FE\% = \frac{2*F*V*C}{Q} *100$$

where F is Faraday's constant (96485 C mol⁻¹), V is the volume of catholyte to be tested for product quantification, C is the HCOO⁻ concentration obtained from NMR analysis of catholyte and Q (integration of current over time for electrolysis period) is the total charge passed through the cathode during electrolysis. Partial formate current density is the product of formate FE and total current density ($j_{formate} = FE_{formate} * j$).

2.5 Computational Methods

Kohn-Sham Density Functional Theory (DFT) studies of each surface were modelled as a 2 × 2 fcc (111) surface slab with five layers where atoms in the bottom two layers were fixed to coordinates from the bulk lattice of the respective alloy, and the remaining atoms were relaxed. Pd₃X (X=Ag, Co, Ni, Cu) skin alloys were represented by substituting 50% of the Pd atoms in the second (subsurface) and fourth layers with X atoms (See Supporting Information for atomic coordinate files of each structure). Electronic energies were calculated using the PBE⁵⁷ exchange correlation functional using the VASP code with projector augmented wave pseudopotentials^{58,59}, and a plane wave basis set was used to represent valence electrons with a 350 eV energy cutoff. An $8 \times 8 \times 1$ Monkhorst-Pack sampling of the k-point grid was employed for each surface. The kpoint sampling and energy cutoffs were found to result in converged energies. The minimum energy configuration of each reference surface was determined iteratively with a conjugate gradient algorithm until the difference in steps was less than 0.1 meV. Band occupancies were broadened using Fermi smearing with a width of 0.4 eV. Spin polarized calculations are reported for the Pd₃Ni and Pd₃Co alloy systems as these were significantly impacted by spin-polarization while the other systems were not.

3. Results and Discussion

An expansive leap in both the distribution of products and product selectivity for the CO₂RR occurred with the transition from bulk polycrystalline metals⁹ to nanostructured materials 15,37,41,44,60-62. This is especially true for Pd. The early work by Hori et al. 1,9 showed CO and H₂ as the major products for CO₂RR on polycrystalline Pd. However, with the shift to carbon supported nanoparticles (Pd/C)^{37,41,44,60,61} and nanostructured thin films⁴⁵, Pd has been shown to reduce CO₂ to formate ion (HCOO⁻) with near perfect selectivity, high faradaic efficiency, at low overpotentials in bicarbonate electrolytes^{37,41,60,61}. We observe similar results for the Pd/C catalyst shown in the transmission electron micrograph (TEM) and scanning electron micrograph (SEM) in Figure 1. Along with high HCOO FEs at low overpotentials, Figure 1(a), we have reproduced the previously observed effect of slow, potential dependent CO poisoning on Pd/C³⁷, Figure 1(b). While the initial reduction current increases with increasing overpotential, the time to deactivation or near complete loss of reduction current due to CO poisoning scales inversely with that trend. This is in line with a progressive switch from the HCOO-HCOOH pathway to the CO dominant pathway with increasing overpotential^{36,38,42}. As has been observed previously³⁷, while the calculated FE for HCOO in these low overpotential regimes is near 100 %, there is a gradual decay in reduction current during constant potential electrolysis, the rate of which increases with increasing reaction overpotential. This decay in reduction current on Pd has been attributed to gradual poisoning of the surface by CO, as Pd has a negative adsorption free energy for CO^{37,63}. While CO is not detected as a reduction product in either the liquid electrolyte or gaseous head space at low overpotential, the slow evolution of CO eventually leads to the passivation of the surface. An additional limitation of Pd/C, as has been shown previously³⁷, is the time dependent sintering of the particles on the carbon support during constant potential electrolysis due to the weak physisorption of the particles onto the carbon. This agglomeration leads to the decrease in

electrochemically active surface area (ECSA) over time with significant losses observed for short periods of constant potential electrolysis³⁷.

To address the limitations of nanostructured Pd catalytic materials, we take advantage of a process known as dealloying to evolve a high surface-to-volume ratio, nanostructured, core-shell Pd alloy electrocatalyst. Through manipulation of dealloying conditions and protocol, precise control of pore size and distribution as well as residual composition and core-shell structure is achieved in a one-step synthesis producre^{64–68}. In addition to the relative simplicity of scaling of the dealloying process, nanoporous metal electrodes are free standing, negating the necessity of carbon supports and eliminating the material agglomeration mechanism as a source of ECSA loss during extended electrolysis. Figure 2 contains SEMs of a set of representative np-PdX electrodes where X = Co, Ni, Cu, and Ag. Care has been taken to ensure that the ligament/pore size of each np-PdX are of order of that of the diameter of the control Pd/C nanoparticles. The residual composition of the dealloyed structure is ~70 atomic % Pd. This composition is an average, as measured by SEM EDAX, and the residual components of the alloy are distributed in a core-shell compositional profile. As shown in the EELS maps in Figures 3 and S2, the surface of the ligaments of the np-PdX are passivated in Pd, while the interior of the ligaments retains a significant fraction of the alloying component. This core-shell compositional profile is a consequence of the dealloying process. Passivation of the surface in the more noble component and preservation of a composition near that of the precursor alloy in the interior of the ligaments is an intrinsic consequence of dealloying 64-68. Dealloying in acidic electrolytes at potentials well above the equilibrium potential of the less noble component drives anodic corrosion and ensures that the surface contains only the more noble component, Pd in this case. The roughness factor (RF), which is proportional to the ECSA, increases with dealloying cycle number (Figure 4). We

note that beyond a certain extent of dealloying (number of cycles), the ECSA as measured by CO stripping begins to decrease, **Figure 4**. We contend that this is due to the competition between movement of the etch front into the bulk of the alloy foil and post-dealloying coarsening behind the etch front which can lead to loss in surface-to-volume ratio^{69–71}. X-Ray photoelectron spectroscopy (XPS) is used to characterize the surface electronic states of the np-PdX electrodes. **Figure S3** shows the peaks corresponding to Pd 3d_{3/2} (high energy band) and 3d_{5/2} (low energy band) spin-orbit states of zero valent Pd for all four alloy electrodes. As shown earlier⁷², the alloying component below the Pd skin lowers the binding energy of Pd 3d_{3/2}. Here, the peak Pd 3d_{3/2} binding energies are 340 eV, 339.6 eV, 339.9 eV, and 339.7 eV and the peak Pd 3d_{5/2} binding energies are 334.7 eV, 334.3 eV, 334.7 eV, and 334.4 eV for np-PdCo, np-PdNi, np-PdCu and np-PdAg respectively, which are all lower than that of pure metallic Pd (3d_{3/2}: 341.1 eV, 3d_{5/2}: 335.42)⁷³. This change in electronic structure of the surface Pd skin directly impacts the adsorption of CO.

Figure 5 contains the cathodic sweep of polarization curves on Pd/C and np-PdCo in Ar purged and CO₂ saturated 1 M KHCO₃. For each electrode, an exponential increase in reductive current density is observed in the absence of CO₂, initiating at approximately 0 V vs. RHE as would be expected for the evolution of H₂ on Pd. In the presence of CO₂, we observe deactivation behavior for Pd/C, np-PdAg, and np-PdCu, **Figures 5** and **S1**. Initially, the reductive current increases as the potential is swept cathodically, but eventually begins a quick decay at potentials beyond -0.5 V vs. RHE. The strong binding of CO on Pd causes fast deactivation as the selectivity switches from HCOO-/HCOOH to CO/H₂ at higher overpotentials ^{36–38,42}. Strikingly, no deactivation is observed in the polarization curves of np-PdNi and np-PdCo, **Figures 5(b)** and **S1**. There are two potential reasons for this: (1) the binding of CO to a Pd-skinned surface with Ni and

Co in the near surface region is weaker than that on Pd, np-PdCu, and np-PdAg; (2) H-binding on np-PdNi and np-PdCo is weaker than that on the other alloys, therefore HER is enhanced. The potential takeaway from this result is that if HCOO selectivity at low overpotential is not altered by the presence of the transition metal alloying component in the bulk and near-surface regions of the Pd-skinned nanocatalyst, the rate of CO poisoning and electrolysis current decay could be significantly reduced.

Figure 6(a) contains the potential dependent FE for HCOO formation in 1 M KHCO₃ for Pd/C, np-PdNi, and np-PdCo. In agreement with previous work^{37,41,42}, Pd-based materials have a near 100% FE for formate at overpotentials below 200 mV, between 0 and -0.2 V vs. RHE. The FE trend for np-PdX closely matches that for Pd/C within this potential range. Figures 6(b) and (c) include the total CO₂RR constant potential electrolysis current density and formate partial current density, respectively. Both np-PdCo and np-PdNi show comparatively high geometric partial current densities for HCOO⁻. Formate partial current densities near 30 mA cm⁻², normalized by geometric area of the electrode, are attained due to the large surface-to-volume ratio of the free standing nanoporous metal electrodes. Figure 7 plots the CO₂RR current density normalized by the real ECSA, determined through CO stripping (Figure 4). At -0.2 V vs. RHE, the electrolysis potential for the data in Figure 7, the FE for HCOO on np-PdNi is essentially 100%. Therefore, the CO₂RR current densities are also the formate partial current densities. The areal, Figure 6(c), and ECSA normalized, Figure 7, formate partial current densities presented here are higher than those reported by others⁴⁷. However, few other reports normalize total and partial CO₂RR currents by the real ECSA, relying on geometric area of the electrode which ignores factors such as nanomaterial morphology and loading. The CO₂RR currents measured at -0.2 V RHE decrease to a stable minimum towards the maximum attainable roughness factor. Depth of porosity, which is

directly proportional to ECSA, does not result in a linear increase in CO₂RR current owing to reactant mass transfer limitations within the tortuous porosity. This phenomena has previously been observed for the oxygen reduction reaction (ORR) on np-PtNi⁷⁴.

In Figure 8 we plot the potentiostatic time-dependent electrolysis current densities for each np-PdX (X = Co, Ni, Cu, Ag) and Pd/C for a range of electrolysis potentials. As with the current density transients measured for Pd/C, Figure 1, the initial current density increases with an increase in overpotential and a concomitant increase in the rate of deactivation is observed, Figures 1 and 8. The rate of deactivation is a strong function of the identity of the transition metal alloying component. Deactivation time increases in the order np-Pd: Ag < Cu < Ni < Co. Deactivation times for np-PdCu and np-PdAg are infeasibly fast, decreasing to nearly zero operational current density in less than 20 minutes at HCOO relevant overpotentials. Within 200 mV overpotential (formate FE ~ 100%), both np-PdNi and np-PdCo show stable poisoning tolerant current densities. Remarkably, np-PdCo exhibits sustained CO2RR current density at all overpotentials tested, up to -0.525 V vs. RHE. In Figure 9, we summarize the deactivation trends by quantifying deactivation as the time required for the CO₂RR current density to decrease to 75% of its original value (t_{75}) . This summarization highlights two trends: (1) rate of deactivation increases with applied overpotential, as previously discussed, and (2) np-PdAg and np-PdCu deactivate at a much faster rate than the other alloys. Combining the potential dependent product selectivity, Figure 6, and rate of deactivation, Figures 8 and 9, we can see that the np-PdX alloys, namely X = Co and Ni, exhibit better CO_2RR electrolysis performance in comparison to Pd/C.

The d-band center of catalytic surface atoms is a common activity descriptor as it is known to scale linearly with the adsorption free energy of reactive intermediates^{75–78}; the further below the Fermi level, the weaker the strength of the bond to adsorbed species. The $\Delta \varepsilon_{d-Pd/Pd_3X}$ trends

as -0.13 Ag < 0.06 Cu < 0.19 Ni < 0.32 Co 75,76 . This trend in d-band center would suggest the following trend in oxygenated intermediate binding strength: Pd₃Ag > Pd₃Cu \approx Pd > Pd₃Ni > Pd₃Co. We have qualitatively assessed the CO binding strength on Pd-skinned Pd₃X (X = Co, Ni, Cu, Ag) alloys through electrochemical CO stripping. **Figure S5** summarizes the electrochemical CO stripping from polycrystalline Pd-skinned Pd₃X (X = Co, Ni, Cu, Ag) alloys in terms of a weighted average of the CO stripping peak potential, the first moment. The first moments of Pd₃Ni and Pd₃Co are lower than those of Pd₃Cu and Pd₃Ag which is indicative of a weaker adsorption of CO on the former, making them more tolerant to CO and resistant to poisoning. As the d-band center shifts downward from the location of Pd, CO adsorption free energy weakens and the time to deactivation increases. Ag is the special case as the d-band center for Pd₃Ag is shifted up from Pd⁷⁵, indicating a stronger interaction. Indeed, we observe fast deactivation of np-PdAg, even in comparison to Pd/C.

Simple d-band models, however, do not always directly correlate to trends in binding energy. This is especially true when lateral adsorbate interactions are significant and in the cases where adsorbates induce changes in the surface or near-surface structure or composition⁷⁹. To assess the impact of alloying and hydrogenation on CO binding, we carried out DFT calculations to determine the low energy adsorption configurations for CO* and H* on Pd and the Pd-skinned alloys. We determined the most stable configurations of different adsorbates on different surfaces by defining the binding energy (BE) for each system as:

$$BE = E_{\rm slab} + n \cdot E_{\rm mol} - E_{\rm ads}$$

where E_{slab} , E_{mol} , and E_{ads} are the DFT energies of a surface slab either clean or containing adsorbed species, a single adsorbate molecule in the gas phase, and the surface slab with all adsorbed species, respectively. Our computational models show that CO* binds most strongly at an hcp site

on pure Pd and at an fcc site for all other surfaces. H* is bound most strongly at an fcc site for all surfaces. Reliably quantifying BEs for these systems under realistic electrochemical conditions is very challenging, but qualitative trends in relative BEs for CO* and H* on a variety of hydrogenated configurations should provide physical insights into the experimental observations.

It is hypothesized that the most active electrocatalysts would exhibit weaker H binding to better facilitate hydrogenations of CO2 into formate as well as weaker CO binding that would result in less CO poisoning. Thus, we modeled CO* on clean surfaces, CO* on hydrogenated surfaces, H* on clean surfaces, and H* on hydrogenated surfaces as well as surfaces with a pre-adsorbed CO to find those with the lowest H and CO binding energies. We investigated the possibility of forming various hydride configurations on these surfaces, including sub-surface hydrides, but all sub-surface hydride cases are found to be higher in energy than the surface adsorbed hydrogen configurations for the Pd alloys. The calculated results are summarized in Figure 10. DFT calculations show that H and CO bind most strongly to clean surfaces (as expected) with magnitudes ranging from 0.46 - 0.62 eV for H and 1.71 - 2.03 eV for CO on all surface models. Furthermore, all binding energies decrease in the presence of co-adsorbed species. Interestingly, the Pd-skin/Pd₃Co system is unique among this group as it yields the weakest binding energies with any low-energy surface configuration. Indeed, the observed trend in calculated H and CO binding energies across these different surfaces straightforwardly follows our experimentally observed trend in formate production and catalyst deactivation.

Furthermore, based on differences in CO binding strengths on the more hydrogenated systems, it appears that higher degrees of hydrogenation effectively destabilize CO binding more so on the Pd-skin/Pd₃Co system relative to the other systems. Past work has shown that selectivity of CO₂ reduction is a function of potential and gradually switches from HCOO⁻/HCOOH to CO/H₂

with increasing overpotentials^{36–38,41,42,55}. The strong potential dependence of the selectivity has been associated with the breakdown of a PdH_x surface hydride phase due to CO_{ad} formation. This hydride breakdown leads to a proportional shift in intermediate selectivity from HCOO_{ad} to COOH_{ad} with increasing overpotential^{41,42,55}. Thus, for the surfaces on which strong CO adsorption is enough to induce the decomposition of the surface hydride, not only would the CO adsorption strength be increased, but the selectivity would also shift toward the CO_{ad} pathway, even at low overpotentials, hastening CO_{ad} passivation. The relatively strong binding of CO to Pd and its alloys ensures fast passivation with CO production, meaning that any shift in selectivity at low overpotential will not be detected as CO in the headspace as the current will quickly decay to zero after only a small amount of CO is formed. The low CO and H BEs on Pd-skin/Pd₃Co calculated using DFT thus help explain the exceptional operational stability of np-PdCo as observed in Figures 8 and 9.

Finally, we wish to comment on the morphological stability of these nanoporous metal catalysts. Comparative CVs before and after CO₂RR load cycling and post-mortem SEMs of the np-PdX electrodes after extended electrolysis at a range of potentials indicate a negligible loss in active area and morphology, **Figures S6** and **S7** respectively. In addition to the morphological stability, these np-PdX electrodes are not susceptible to delamination, loss of contact between carbon supported catalyst and current collector, as is common with ionic polymer mixed, agglomerated carbon-supported composite electrodes⁸⁰. While increasing ionomer contents improves the durability of these agglomerated electrodes, it is offset by activity losses associated with active site blocking and electrode impedance⁸¹. These results highlight the utility of nanoporous metal electrodes where high aerial partial current densities and selectivity for HCOO-

are combined with an electrochemical and morphological stability that cannot be matched by nanoparticulate based CO₂RR electrocatalysts.

4. Conclusions

In summary, we have presented the development of np-PdX (X = Ag, Cu, Ni, Co) catalytic electrodes, where np-PdCo and np-PdNi show selective and stable electrolytic evolution of HCOOfrom CO₂ with areal HCOO current densities greater than 20 mA cm⁻². Traditional Pd/C electrocatalysts, while generating HCOO at low overpotential with high FE, quickly deactivate, even with a low ratio of COOHad/HCOOad intermediate favorability, due to the large negative adsorption free energy of CO on Pd. In contrast, np-PdNi and np-PdCo show stable currents at overpotentials below 200 mV producing HCOO with near 100% selectivity. Additionally, np-PdCo exhibits stable CO₂RR current densities at overpotentials as high as 500 mV. The np-PdX electrodes are characterized by a core-shell structure, formed intrinsically through the dealloying process, and an interconnected, bicontinuous morphology that possesses a high surface-to-volume nanostructure in a free-standing form factor. The rate of CO₂RR deactivation at potentials at which HCOO FEs approach 100% is found to trend with the identity of the alloying component: np-PdAg > np-PdCu > Pd/C > np-PdNi > np-PdCo. This trend in deactivation is a convolution of the CO adsorption strength, manipulated by electronic effects associated with the presence of transition metal alloying components near the Pd-skin surface, and a compositional dependent change in the near surface H-sorption capacity. Transition metal alloying components below the Pd-skin surface act to destabilize subsurface H and change the relative binding of surface adsorbed H* and CO* in a range of adsorption configurations. The Pd-skinned np-PdCo and np-PdNi are found to have low CO and H BEs which results in selective electrohydrogenation of CO₂ to HCOO at low overpotential and tolerance to CO poisoning. The overall result is HCOO selectivity at low

overpotentials with high areal and ECSA normalized HCOO partial current densities and improved operational durability during constant potential electrolysis.

Supporting Information:

Method of determining ECSA, Ar/CO₂ purged polarization curves, EELS mapping of np-PdX, XPS of Pd₃X, CO stripping of np-PdX, Ar purged CVs before and after CO₂RR electrolysis, Postmorten SEM of np-PdX after CO₂RR electrolysis, DFT calculation details. This information is available free of charge on the ACS Publications website.

Acknowledgements:

SC and JS acknowledge financial support from ACS PRF award #57565-DNI5. JLH and MLT acknowledge financial support from NSF MRI award #1429661. CG and JK acknowledge support from the R.K. Mellon Foundation and the Irving Wender Fellowship through the Department of Chemical and Petroleum Engineering at the University of Pittsburgh. CG and JK also acknowledgment support from ACS PRF award #55595-DNI4 and the National Science Foundation award #CBET-1653392. We thank the University of Pittsburgh Center for Research Computing for computing time and technical support.

References:

- Hori, Y., Wakebe, H., Tsukamoto, T. & Koga, O. Electrocatalytic process of CO selectivity in electrochemical reduction of CO2 at metal electrodes in aqueous media.
 Electrochim. Acta 1994, 39, 1833–1839.
- 2. Whipple, D. T. & Kenis, P. J. A. Prospects of CO2 utilization via direct heterogeneous electrochemical reduction. *J. Phys. Chem. Lett.* **2010**, *1*, 3451–3458.

- 3. Costentin, C., Robert, M. & Savéant, J.-M. Catalysis of the electrochemical reduction of carbon dioxide. *Chem. Soc. Rev.* **2013**, *42*, 2423–36.
- 4. Schouten, K., Kwon, Y., van der Ham, C., Qin, Z., Koper, M. A new mechanism for the selectivity to C1 and C2 species in the electrochemical reduction of carbon dioxide on copper electrodes. *Chem. Sci.* **2011**, *2*, 1902–1909.
- 5. Peterson, a., Abild-Pedersen, F., Studt, F., Rossmeisl, J., Norskov, J. How copper catalyzes the electroreduction of carbon dioxide into hydrocarbon fuels. *Energy Environ. Sci.* **2010**, *3*, 1311–1315.
- 6. Kuhl, K., Hatsukade, T., Cave, E., Abram, D., Kibsgaard, J., Jaramillo, T. Electrocatalytic conversion of carbon dioxide to methane and methanol on transition metal surfaces. *J. Am. Chem. Soc.* **2014**, *136*, 14107–14113.
- 7. Kuhl, K., Cave, E., Abram, D., Jaramillo, T. New insights into the electrochemical reduction of carbon dioxide on metallic copper surfaces. *Energy Environ. Sci.* **2012**, *5*, 7050–7059.
- 8. Gattrell, M., Gupta, N., Co, A. A review of the aqueous electrochemical reduction of CO2 to hydrocarbons at copper. *J. Electroanal. Chem.* **2006**, *594*, 1–19.
- 9. Hori, Y. Electrochemical CO2 Reduction on Metal Electrodes. in *Modern Aspects of Electrochemistry* (Springer, 2008). 89–189.
- 10. Peterson, A., Norskov, J. Activity descriptors for CO2 electroreduction to methane on transition-metal catalysts. *J. Phys. Chem. Lett.* **2012**, *3*, 251–258.
- 11. Nie, X., Esopi, M., Janik, M., Asthagiri, A. Selectivity of CO2 reduction on copper electrodes: The role of the kinetics of elementary steps. *Angew. Chem. Int. Ed.* **2013**, *52*, 2459–2462.

- 12. Medina-Ramos, J., DiMeglio, J., Rosenthal, J. Efficient Reduction of CO2 to CO with High Current Density Using in Situ or ex Situ Prepared Bi-Based Materials. *J. Am. Chem. Soc.* **2014**, *136*, 8361–8367.
- 13. Kas, R., Kortlever, R., Yilmaz, H., Koper, M. T. M. & Mul, G. Manipulating the Hydrocarbon Selectivity of Copper Nanoparticles in CO2 Electroreduction by Process Conditions. *ChemElectroChem* **2015**, *2*, 354–358.
- Wang, X., Varela, A. S., Bergmann, A., Kühl, S. & Strasser, P. Catalyst Particle Density Controls Hydrocarbon Product Selectivity in CO2Electroreduction on CuOx. ChemSusChem 2017, 10, 4642–4649.
- Zhang, W., Hu, Y., Ma, L., Zhu, G., Wang, Y., Xue, X., Chen, R., Yang, S., Jin, Z.
 Progress and Perspective of Electrocatalytic CO2 Reduction for Renewable Carbonaceous
 Fuels and Chemicals. Adv. Sci. 2018, 5, 1700275.
- 16. Kortlever, R., Shen, J., Schouten, K. J. P., Calle-Vallejo, F. & Koper, M. T. M. Catalysts and Reaction Pathways for the Electrochemical Reduction of Carbon Dioxide. *J. Phys. Chem. Lett.* **2015**, *6*, 4073–4082.
- 17. Azuma, M. & Watanabe, M. Electrodes in Low-Temperature Aqueous KHC03 Media. **1990**, *137*, 1772–1778.
- 18. Kortlever, R., Balemans, C., Kwon, Y. & Koper, M. T. M. Electrochemical CO2 reduction to formic acid on a Pd-based formic acid oxidation catalyst. *Catal. Today* **2015**, *244*, 58–62.
- 19. Lu, X., Leung, D., Wang, H., Leung, M., Xuan, J. Electrochemical Reduction of Carbon Dioxide to Formic Acid. *ChemElectroChem* **2014**, *1*, 836–849.
- 20. Rosen, J., Hutchings, G., Lu, Q., Rivera, S., Zhou, Y., Vlachos, D., Jiao, F. Mechanistic

- Insights into the Electrochemical Reduction of CO2 to CO on Nanostructured Ag Surfaces. *ACS Catal.* **2015**, *5*, 4293–4299.
- 21. Back, S., Yeom, M., Jung, Y. Active Sites of Au and Ag Nanoparticle Catalysts for CO2 Electroreduction to CO. *ACS Catal.* **2015**, *5*, 5089–5096.
- Rosen, J., Hutchings, G., Lu, Q., Rivera, S., Zhou, Y., Valchos, D., Jiao, F. Mechanistic Insights into the Electrochemical Reduction of CO2 to CO on Nanostructured Ag Surfaces. ACS Catal. 2015, 5, 4293–4299.
- Zhu, W., Michalsky, R., Metin, O., Lv, H., Guo, S., Wright, C., Sun, X., Peterson, A.,
 Sun, S. Monodisperse Au nanoparticles for selective electrocatalytic reduction of CO2 to
 CO. J. Am Chem. Soc. 2013, 135, 16833–16836.
- Zhang, H., Ma, Y., Quan, F., Huang, J., Jia, F., Zhang, L. Selective electro-reduction of CO2 to formate on nanostructured Bi from reduction of BiOCl nanosheets. *Electrochem*. *Comm.* 2014, 46, 63–66.
- 25. Zhang, S., Kang, P. & Meyer, T. J. Nanostructured tin catalysts for selective electrochemical reduction of carbon dioxide to formate. *J Am Chem Soc* 2014, 136, 1734– 1737.
- 26. Detweiler, Z. M., White, J. L., Bernasek, S. L. & Bocarsly, A. B. Anodized indium metal electrodes for enhanced carbon dioxide reduction in aqueous electrolyte. *Langmuir* **2014**, *30*, 7593–7600.
- 27. Vo, T., Purohit, K., Nguyen, C., Biggs, B., Mayoral, S., Haan, H. Formate: An Energy Storage and Transport Bridge between Carbon Dioxide and a Formate Fuel Cell in a Single Device. *ChemSusChem* **2015**, *8*, 3853–3858.
- 28. El-Nagar, G. A., Hassan, M. A., Lauermann, I. & Roth, C. Efficient Direct Formic Acid

- Fuel Cells (DFAFCs) Anode Derived from Seafood waste: Migration Mechanism. *Sci. Rep.* **2017**, *7*, 17818.
- 29. Miesse, C., Jung, W., Jeong, K., Lee, J., Lee, J., Han, J., Yoon, S., Nam, S., Lim, T., Hong, S. Direct formic acid fuel cell portable power system for the operation of a laptop computer. *J. Power Sources* **2006**, *162*, 532–540.
- 30. Yu, X. & Pickup, P. G. Recent advances in direct formic acid fuel cells (DFAFC). *Journal of Power Sources* **2008**, *182*, 124–132.
- 31. Yan, B., Concannon, N. M., Milshtein, J. D., Brushett, F. R. & Surendranath, Y. A Membrane-Free Neutral pH Formate Fuel Cell Enabled by a Selective Nickel Sulfide Oxygen Reduction Catalyst. *Angew. Chemie Int. Ed.* **2017**, *56*, 7496–7499.
- 32. Aloisio, S., Hintze, P. E. & Vaida, V. The hydration of formic acid. *J. Phys. Chem. A* **2002**, *106*, 363–370.
- Qi, X., Li, H.-P. & Wu, X.-F. A Convenient Palladium-Catalyzed Carbonylative Synthesis of Benzofuran-2(3 H)-ones with Formic Acid as the CO Source. *Chem. An Asian J.*2016, 11, 2453–2457.
- 34. Chauvier, C., Tlili, A., Das Neves Gomes, C., Thuéry, P. & Cantat, T. Metal-free dehydrogenation of formic acid to H₂ and CO₂ using boron-based catalysts. *Chem. Sci.* **2015**, *6*, 2938–2942.
- 35. Long, B., Long, Z., Wang, Y., Tan, X., Hang, Y., Long, C., Qin, S., Zhang, W. Formic Acid Catalyzed Gas-Phase Reaction of H2O with SO3 and the Reverse Reaction: A Theoretical Study. *ChemPhysChem* **2012**, *13*, 323–329.
- 36. Gao, D., Zhou, H., Wang, J., Miao, S., Yang, F., Wang, G., Wang, J., Bao, X. Size-Dependent Electrocatalytic Reduction of CO2 over Pd Nanoparticles. *J Am Chem Soc*

- **2015**, *137*, 4288–4291.
- Min, X. & Kanan, M. W. Pd-Catalyzed Electrohydrogenation of Carbon Dioxide to Formate: High Mass Activity at Low Overpotential and Identification of the Deactivation Pathway. J. Am. Chem. Soc. 2015, 137, 4701–4708.
- 38. Sheng, W., Kattel, S., Yao, S., Yan, B., Liang, Z., Hawxhurst, C., Wu, Q., Chen, J. Electrochemical Reduction of CO2 to Synthesis Gas with Controlled CO/H2 Ratios. *Energy Environ. Sci.* **2017**, *10*, 1180–1185.
- 39. Kortlever, R., Peters, I., Koper, S. & Koper, M. T. M. Electrochemical CO2 Reduction to Formic Acid at Low Overpotential and with High Faradaic Efficiency on Carbon-Supported Bimetallic Pd-Pt Nanoparticles. *ACS Catal.* **2015**, *5*, 3916–3923.
- 40. Humphrey, J., Plana, D., Celorrio, V., Sadasivan, S., Tooze, R., Rodriguez, P., Fermin, D. Electrochemical Reduction of Carbon Dioxide at Gold-Palladium Core-Shell Nanoparticles: Product Distribution versus Shell Thickness. *ChemCatChem* 2016, 8, 952–960.
- 41. Gao, D., Zhou, H., Cai, F., Wang, J., Wang, G., Bao, X. Pd-Containing Nanostructures for Electrochemical CO2 Reduction Reaction. *ACS Catal.* **2018**, *8*, 1510–1519.
- 42. Gao, D., Zhou, H., Cai, F., Wang, D., Hu, Y., Jiang, B., Cai, W., Chen, X., Si, R., Yang, F., Miao, S., Wang, J., Wang, G., Bao, X. Switchable CO2 electroreduction via engineering active phases of Pd nanoparticles. *Nano Res.* **2017**, *10*, 2181–2191.
- 43. Gabrielli, C., Grand, P. P., Lasia, A. & Perrot, H. Investigation of Hydrogen Adsorption and Absorption in Palladium Thin Films. *J. Electrochem. Soc.* **2004**, *151*, A1937.
- 44. Rahaman, M., Dutta, A. & Broekmann, P. Size-Dependent Activity of Palladium Nanoparticles: Efficient Conversion of CO 2 into Formate at Low Overpotentials.

- ChemSusChem 2017, 10, 1733–1741.
- 45. Zhou, F., Li, H., Fournier, M. & MacFarlane, D. R. Electrocatalytic CO 2 Reduction to Formate at Low Overpotentials on Electrodeposited Pd Films: Stabilized Performance by Suppression of CO Formation. *ChemSusChem* **2017**, *10*, 1509–1516.
- 46. Tang, Q., Lee, Y., Li, D., Choi, W., Liu, C., Lee, D., Jiang, D. Lattice Hydride Mechanism in Electrocatalytic CO2 Reduction by Structurally Precise Copper-Hydride Nanoclusters.
 J. Am Chem. Soc. 2017, 139, 9728–9736.
- Klinkova, A., Luna, P., Dinh, C., Voznyy, O., Larin, E., Kumacheva, E., Sargent, E.
 Rational Design of Efficient Palladium Catalysts for Electroreduction of Carbon Dioxide to Formate. ACS Catal. 2016, 6, 8115–8120.
- 48. Takashima, T., Suzuki, T. & Irie, H. Electrochemical carbon dioxide reduction on copper-modified palladium nanoparticles synthesized by underpotential deposition. *Electrochim.*Acta 2017, 229, 415–421.
- 49. Zhao, Z. & Lu, G. Computational Screening of Near-Surface Alloys for CO2 Electroreduction. *ACS Catal.* **2018**, *8*, 3885–3894.
- 50. Zhu, W., Zhang, L., Yang, P., Chang, X., Dong, H., Li, A., Hu, C., Huang, Z., Zhao, Z., Gong, J. Morphological and Compositional Design of Pd-Cu Bimetallic Nanocatalysts with Controllable Product Selectivity toward CO2 Electroreduction. *Small* 2018, 14, 1703314.
- 51. Li, M., Wang, J., Li, P., Chang, K., Li, C., Wang, T., Jiang, B., Zhang, H., Liu, H., Yamauchi, Y., Umezawa, N., Ye, J. Mesoporous palladium–copper bimetallic electrodes for selective electrocatalytic reduction of aqueous CO2 to CO. *J. Mater. Chem. A* **2016**, *4*, 4776–4782.

- 52. Kim, S., Park, M., Kim, H., Yoon, K., Son, J., Lee, J., Kim, B., Lee, J., Hong, J. In-situ nano-alloying Pd-Ni for economical control of syngas production from high-temperature thermo-electrochemical reduction of steam/CO2. *Appl. Catal. B Environ.* **2017**, *200*, 265–273.
- 53. Tao, H., Sun, X., Back, S., Han, Z., Zhu, Q., Robertson, A., Ma, T., Fan, Q., Han, B., Jung, Y., Sun, Z. Doping Palladium with Tellurium for Highly Selective Electrocatalytic Reduction of Aqueous CO2 to CO. *Chem. Sci.* 2018, 9, 483–487.
- 54. Bai, X., Chen, W., Zhao, C., Li, S., Song, Y., Ge, R., Wei, W., Sun, Y. Exclusive Formation of Formic Acid from CO2Electroreduction by a Tunable Pd-Sn Alloy. *Angew. Chem. Int. Ed.* **2017**, *56*, 12219–12223.
- 55. Jiang, B., Zhang, X.-G., Jiang, K., Wu, D.-Y. & Cai, W.-B. Boosting Formate Production in Electrocatalytic CO 2 Reduction over Wide Potential Window on Pd Surfaces. *J Am Chem Soc* **2018**, *140*, 2880–2889.
- 56. Mazumder, V. & Sun, S. Oleylamine-mediated synthesis of Pd nanoparticles for catalytic formic acid oxidation. *J. Am. Chem. Soc.* **2009**, *131*, 4588–4589.
- 57. Perdew, J. P., Burke, K. & Ernzerhof, M. Generalized gradient approximation made simple. *Phys. Rev. Lett.* **1996**, *77*, 3865–3868.
- 58. Mortensen, J. J., Hansen, L. B. & Jacobsen, K. W. Real-space grid implementation of the projector augmented wave method. *Phys. Rev. B* **2005**, *71*, 1–11.
- 59. Kresse, G. & Furthmüller, J. Efficient iterative schemes for ab initio total-energy calculations using a plane-wave basis set. *Phys. Rev. B* **1996**, *54*, 11169–11186.
- 60. Kortlever, R., Peters, I., Koper, M. Electrochemical CO2 reduction to formic acid at low overpotential and with high faradaic efficiency on carbon supported bimetallic Pd-Pt

- nanoparticles. ACS Catal. 2015, 5, 3916–3923.
- Gao, D., Zhou, H., Wang, J., Miao, S., Yang, F., Wang, G., Wang, J., Bao, X. Size-Dependent Electrocatalytic Reduction of CO2 over Pd Nanoparticles. *J. Am Chem. Soc.* 2015, 137, 4288–4291.
- 62. Humphrey, J., Plana, D., Celorrio, V., Sadasivan, S., Tooze, R., Rodriguez, P., Fermin, D. Electrochemical Reduction of Carbon Dioxide at Gold-Palladium Core-Shell Nanoparticles: Product Distribution versus Shell Thickness. *ChemCatChem* **2016**, *8*, 952–960.
- 63. Zhang, H. X., Wang, S. H., Jiang, K., André, T. & Cai, W. Bin. In situ spectroscopic investigation of CO accumulation and poisoning on Pd black surfaces in concentrated HCOOH. *J. Power Sources* **2012**, *199*, 165–169.
- 64. Li, X., Chen, Q., McCue, I., Snyder, J., Crozier, P., Erlebacher, J., Sieradzki, K. Dealloying of noble-metal alloy nanoparticles. *Nano Lett.* **2014**, *14*, 2569–2577.
- 65. Snyder, J., Livi, K., Erlebacher, J. Dealloying Silver/Gold Alloys in Neutral Silver Nitrate Solution: Porosity Evolution, Surface Composition, and Surface Oxides. *J. Electrochem. Soc.* **2008**, *155*, C464–C473.
- 66. Erlebacher, J. An Atomistic Description of Dealloying. *J. Electrochem. Soc.* **2004**, *151*, C614–C626.
- 67. Snyder, J., Asanithi, P., Dalton, A. B. & Erlebacher, J. Stabilized nanoporous metals by dealloying ternary alloy precursors. *Adv. Mater.* **2008**, *20*, 4883–4886.
- 68. Snyder, J., McCue, I., Livi, K., Erlebacher, J. Structure/Processing/Properties relationships in nanoporous nanoparticles as applied to catalysis of the cathodic oxygen reduction reaction. *J. Am. Chem. Soc.* **2012**, *134*, 8633–8645.

- 69. Luo, X., Li, R., Huang, L. & Zhang, T. Nucleation and growth of nanoporous copper ligaments during electrochemical dealloying of Mg-based metallic glasses. *Corros. Sci.* **2013**, *67*, 100–108.
- 70. Fujita, T. Hierarchical nanoporous metals as a path toward the ultimate three-dimensional functionality. *Sci. Technol. Adv. Mater.* **2017**, *18*, 724–740.
- 71. Kertis, F., Snyder, J., Govada, L., Khurshid, S., Chayen, N., Erlebacher, J. Structure/Processing Relationships in the Fabrication of Nanoporous Gold. *JOM* **2010**, *62*, 50–56.
- 72. Chen, L., Guo, H., fujita, T., Hirata, A., Zheng, W., Inoue, A., Chen, M. Nanoporous PdNi bimetallic catalyst with enhanced electrocatalytic performances for electro-oxidation and oxygen reduction reactions. *Adv. Funct. Mater.* **2011**, *21*, 4364–4370.
- 73. Naumkin, A., Kraut-Vass, A., Gaarenstroom, S., Powell, C. NIST X-ray Photoelectron Spectroscopy Database. **2012**, Available at: http://dx.doi.org/10.18434/T4T88K%09.
- 74. Snyder, J., Fujita, T., Chen, M., Erlebacher, J. Oxygen reduction in nanoporous metal-ionic liquid composite electrocatalysts. *Nat. Mater.* **2010**, *9*, 904–907.
- 75. Xin, H., Vojvodic, A., Voss, J., Nørskov, J. K. & Abild-Pedersen, F. Effects of d-band shape on the surface reactivity of transition-metal alloys. *Phys. Rev. B* **2014**, *89*, 115114.
- 76. Ou, L. Design of Pd-Based Bimetallic Catalysts for ORR: A DFT Calculation Study. *J. Chem.* **2015**, *2015*, 1–11.
- 77. Norskov, J. K., Abild-Pedersen, F., Studt, F. & Bligaard, T. Density functional theory in surface chemistry and catalysis. *Proc. Natl. Acad. Sci.* **2011**, *108*, 937–943.
- 78. Stamenkovic, V., Mun, B., Mayrhofer, K., Ross, P., Markovic, N., Rossmeisl, J., Greeley, J., Norskov, J. Changing the Activity of Electrocatalysts for Oxygen Reduction by Tuning

- the Surface Electronic Structure. Angew. Chem. Int. Ed. 2006, 118, 2963-2967.
- 79. Xin, H. & Linic, S. Communications: Exceptions to the d-band model of chemisorption on metal surfaces: The dominant role of repulsion between adsorbate states and metal d-states. *J. Chem. Phys.* **2010**, *132*, 221101.
- 80. Yuan, X. Z., Li, H., Zhang, S., Martin, J. & Wang, H. A review of polymer electrolyte membrane fuel cell durability test protocols. *Journal of Power Sources* **2011**, *196*, 9107–9116.
- 81. Sasikumar, G., Ihm, J. W. & Ryu, H. Dependence of optimum Nafion content in catalyst layer on platinum loading. *J. Power Sources* **2004**, *132*, 11–17.

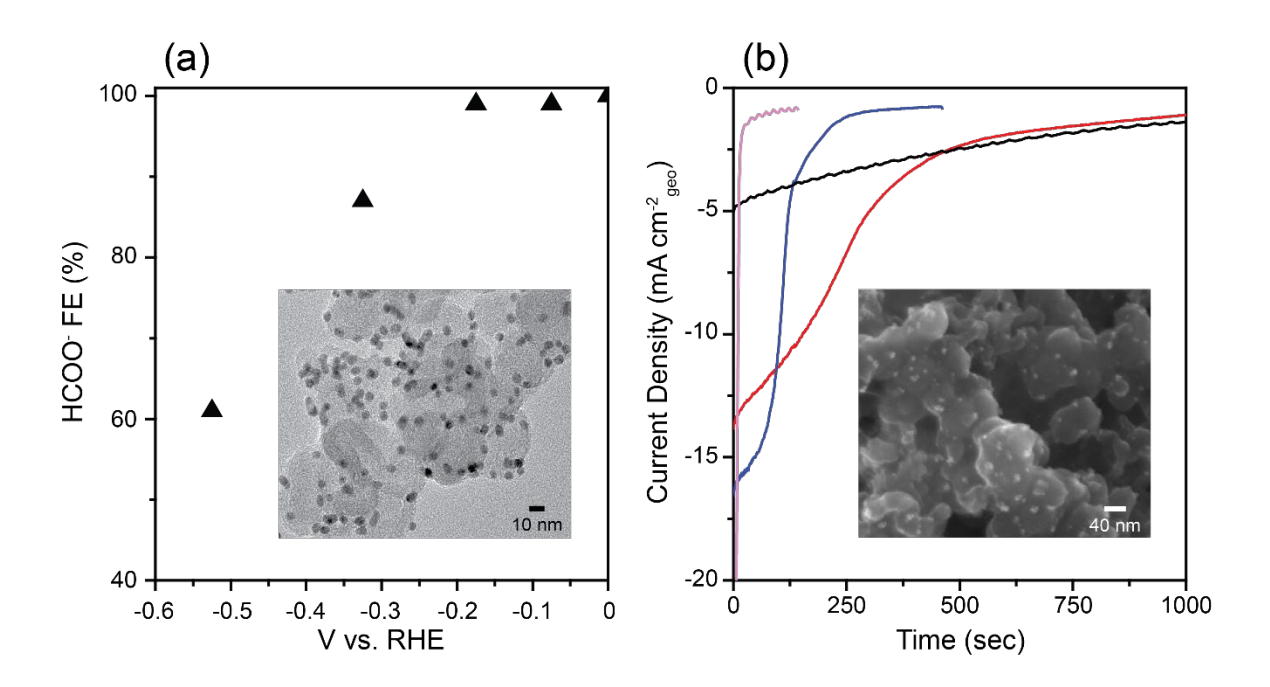


Figure 1: (a) HCOO⁻ FE for Pd/C measured through constant potential electrolysis in CO₂ saturated 1 M KHCO₃. Inset: TEM of as-synthesized Pd/C, prior to electrolysis. (b) CO₂RR current density in CO₂ saturated 1 M KHCO₃ at -0.175 V (black), -0.325 V (red), -0.425 V (blue), -0.525 V (pink) vs. RHE. Inset: SEM of Pd/C post-electrolysis.

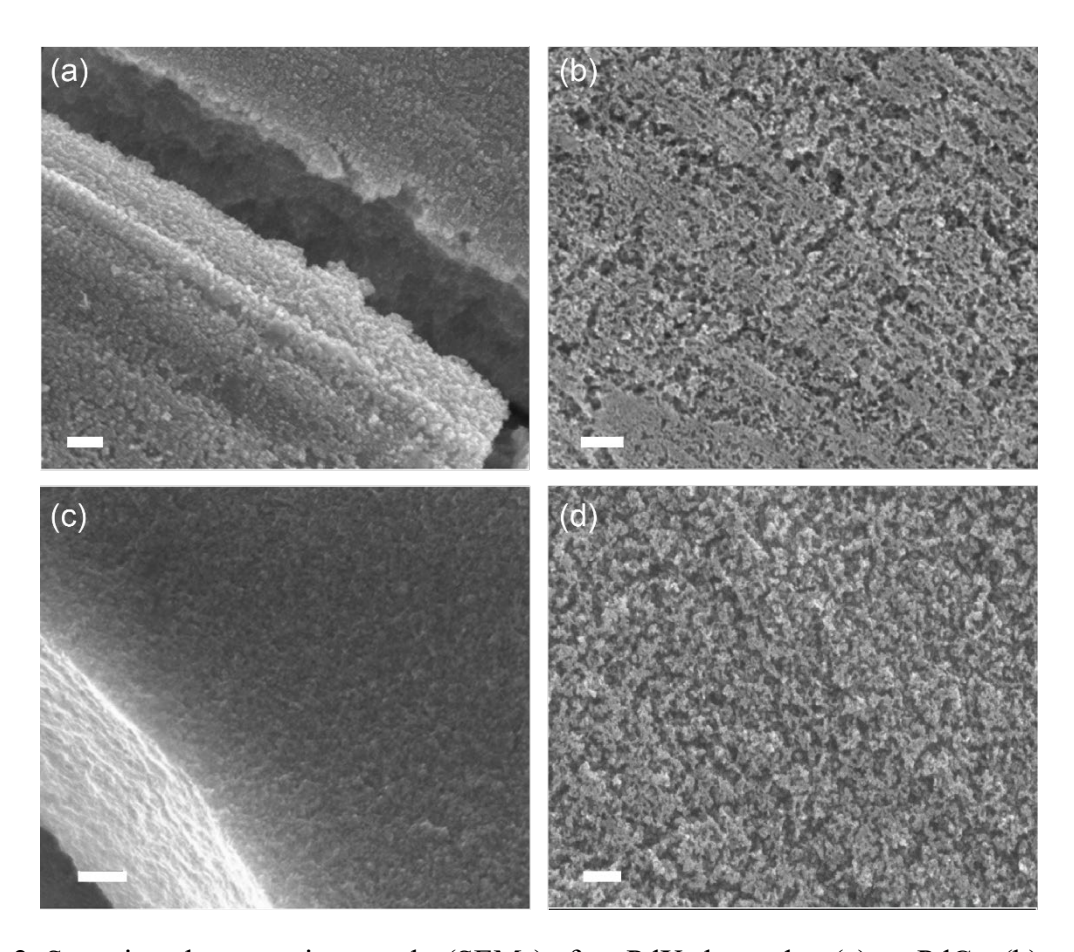


Figure 2: Scanning electron micrographs (SEMs) of np-PdX electrodes. (a) np-PdCo, (b) np-PdNi, (c) np-PdAg, (d) np-PdCu. Scalebars are 100 nm.

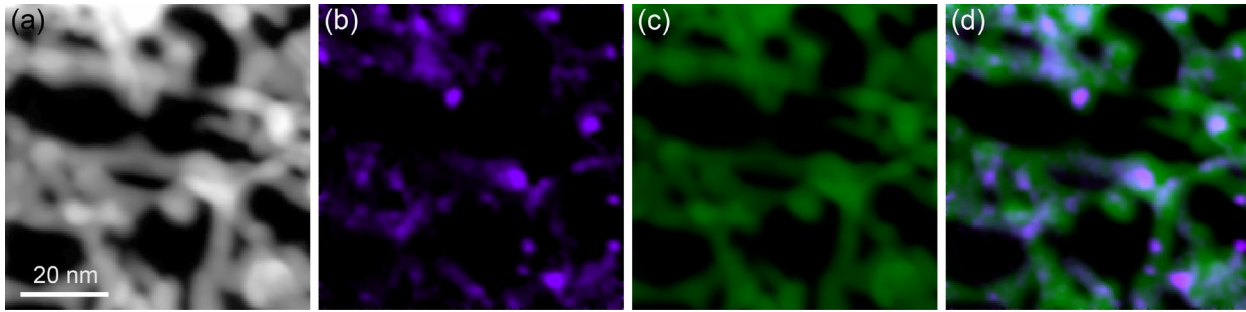


Figure 3: HAADF-STEM images of (a) np-PdCo and their corresponding (b) Co (violet), (c) Pd (green), and (d) composite EELS maps.

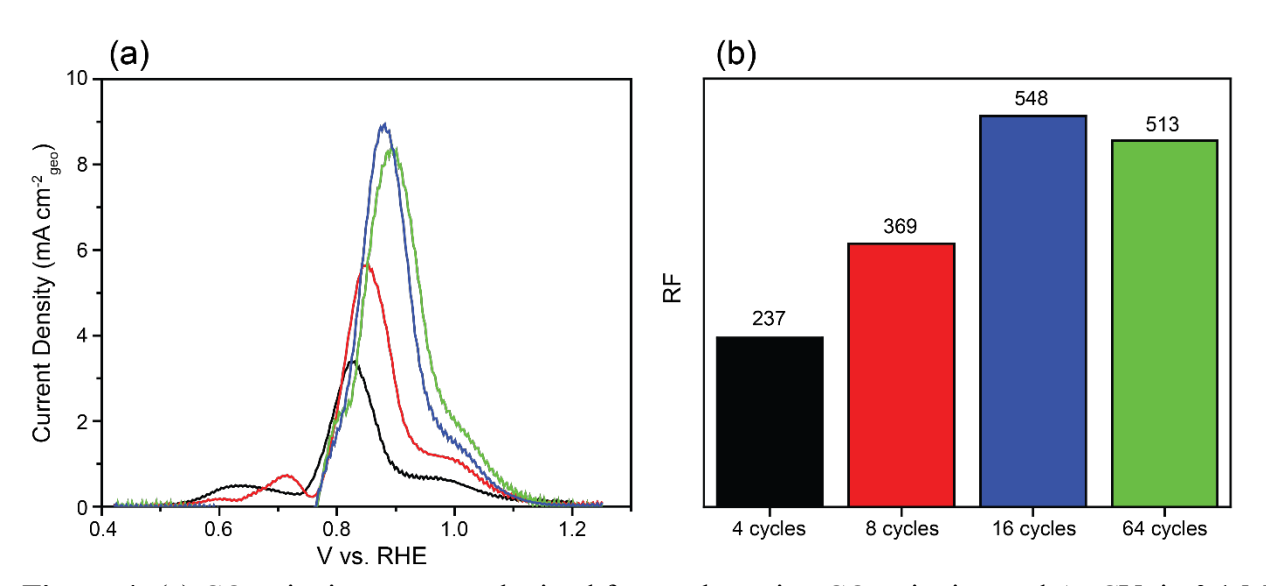


Figure 4: (a) CO stripping current, obtained from subtracting CO stripping and Ar CV, in 0.1 M HClO₄ on np-PdNi as a function of dealloying cycle number (dealloyed depth); 4 cycles (black), 8 cycles (red), 16 cycles (blue), 64 cycles (green). (b) Roughness factor (RF) for each dealloyed depth.

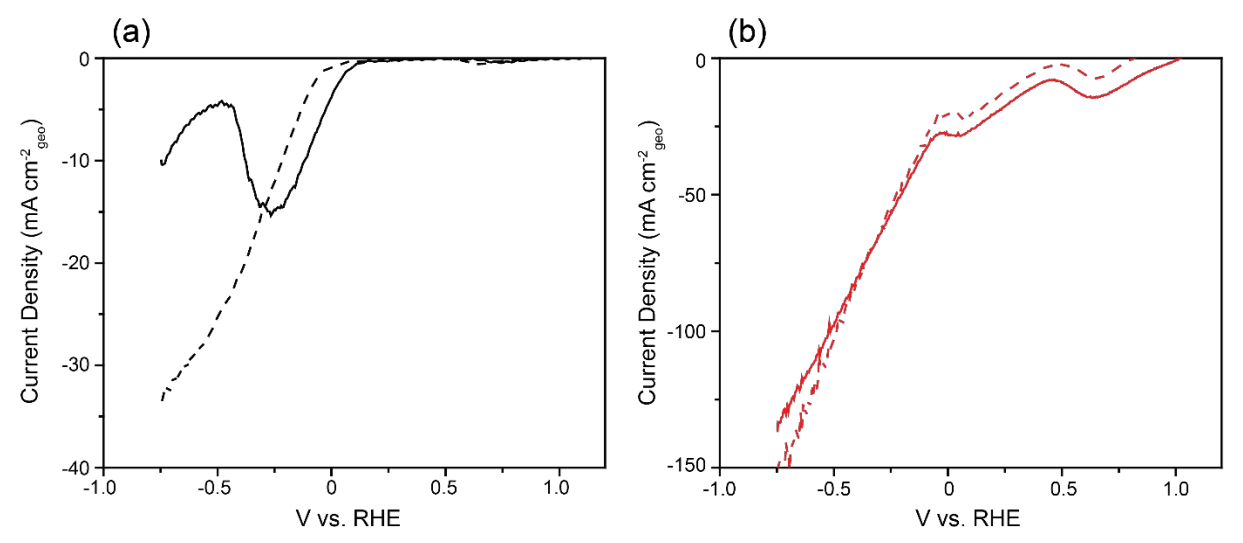


Figure 5: (a) Polarization curve in Ar purged (dashed line) and CO₂ saturated (solid line)1M KHCO₃ for Pd/C. (b) Polarization curve in Ar purged (dashed line) and CO₂ saturated (solid line) 1M KHCO₃ for np-PdCo. Scan rate is 10 mV s⁻¹.

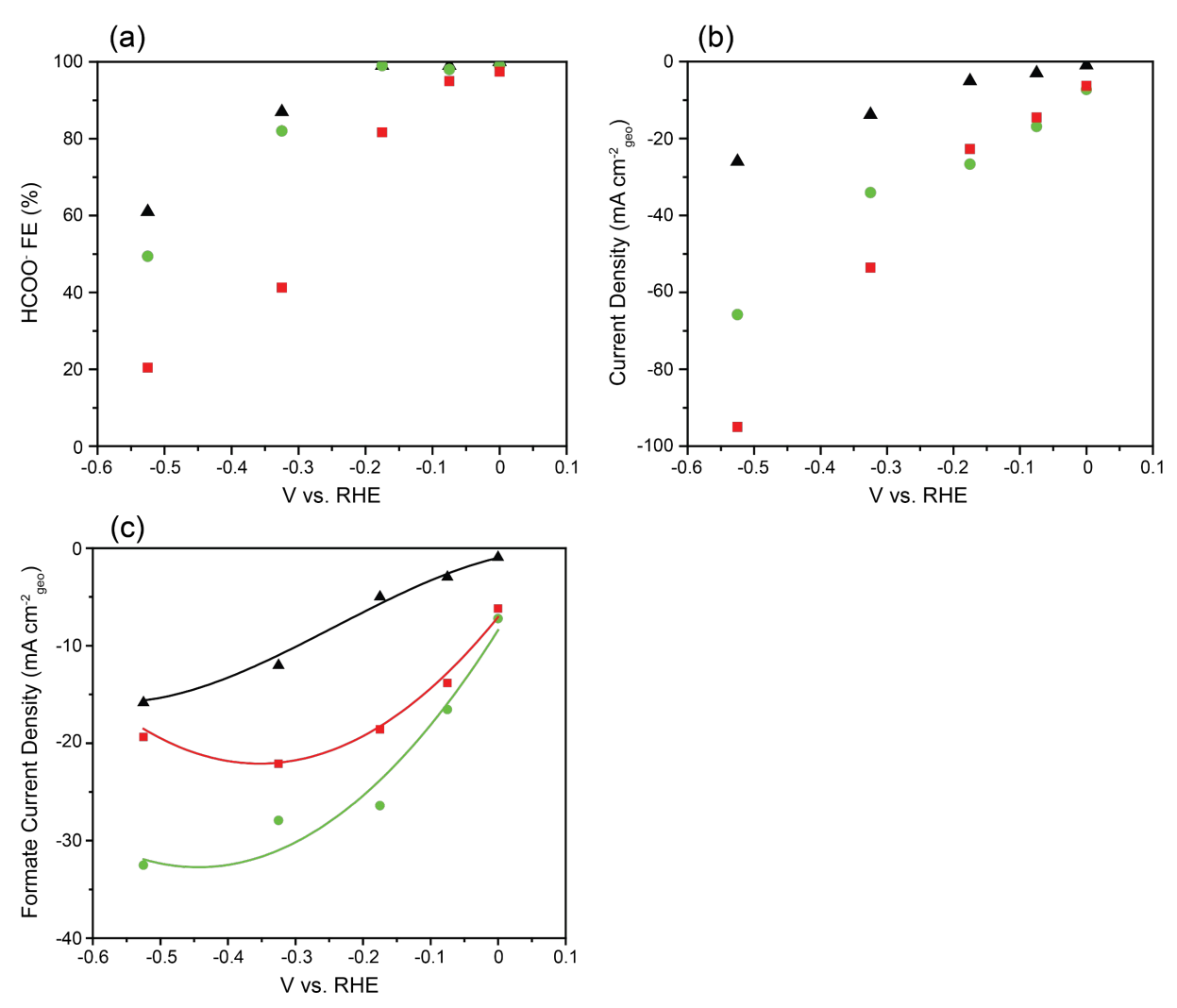


Figure 6: (a) HCOO⁻ faradaic efficiency as a function of CO₂RR electrolysis potential for Pd/C (black triangle), np-PdNi (green circle), and np-PdCo (red square). (b) Total CO₂RR steady-state current normalized by the geometric area of the electrode for Pd/C (black triangle), np-PdNi (green circle), and np-PdCo (red square). (c) Formate partial current density for Pd/C (black triangle), np-PdNi (green circle), and np-PdCo (red square). All data recorded in CO₂ saturated 1 M KHCO₃.

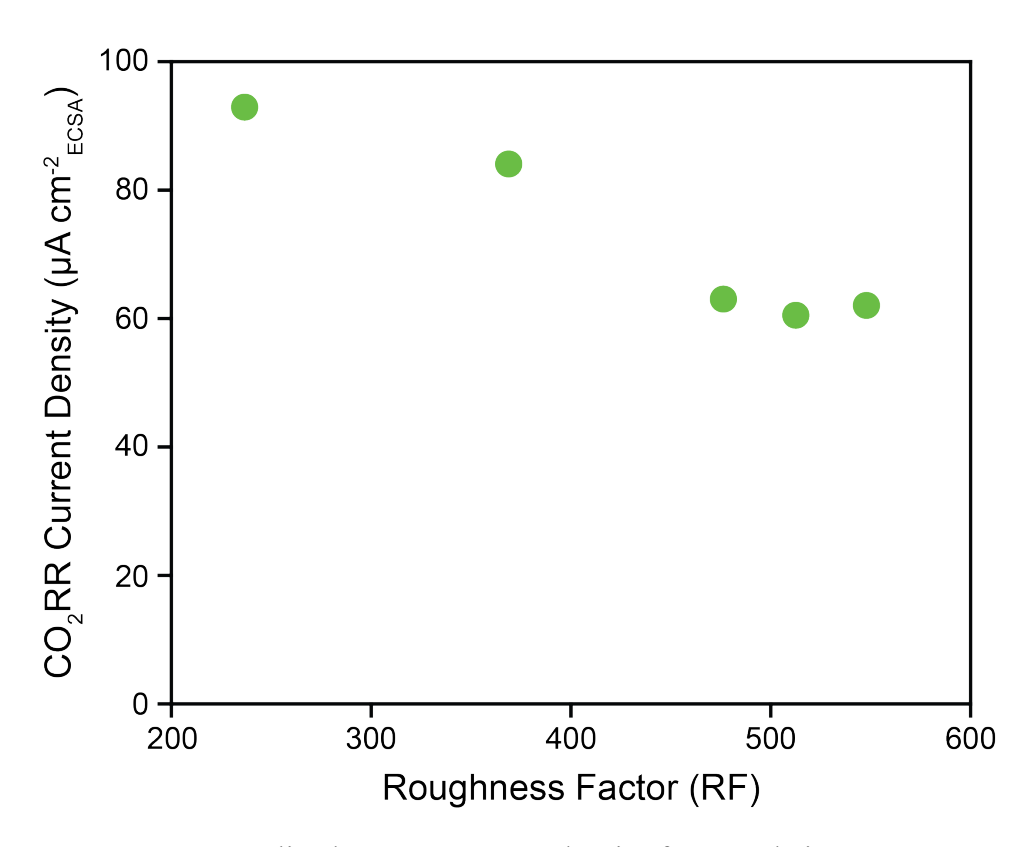


Figure 7: ECSA normalized CO₂RR current density for np-PdNi at -0.2 V vs. RHE in CO₂ saturated 1 M KHCO₃ as a function of dealloyed depth, roughness factor (RF). ECSA and RF determined by integration of CO stripping current, **Figure 4(a)**.

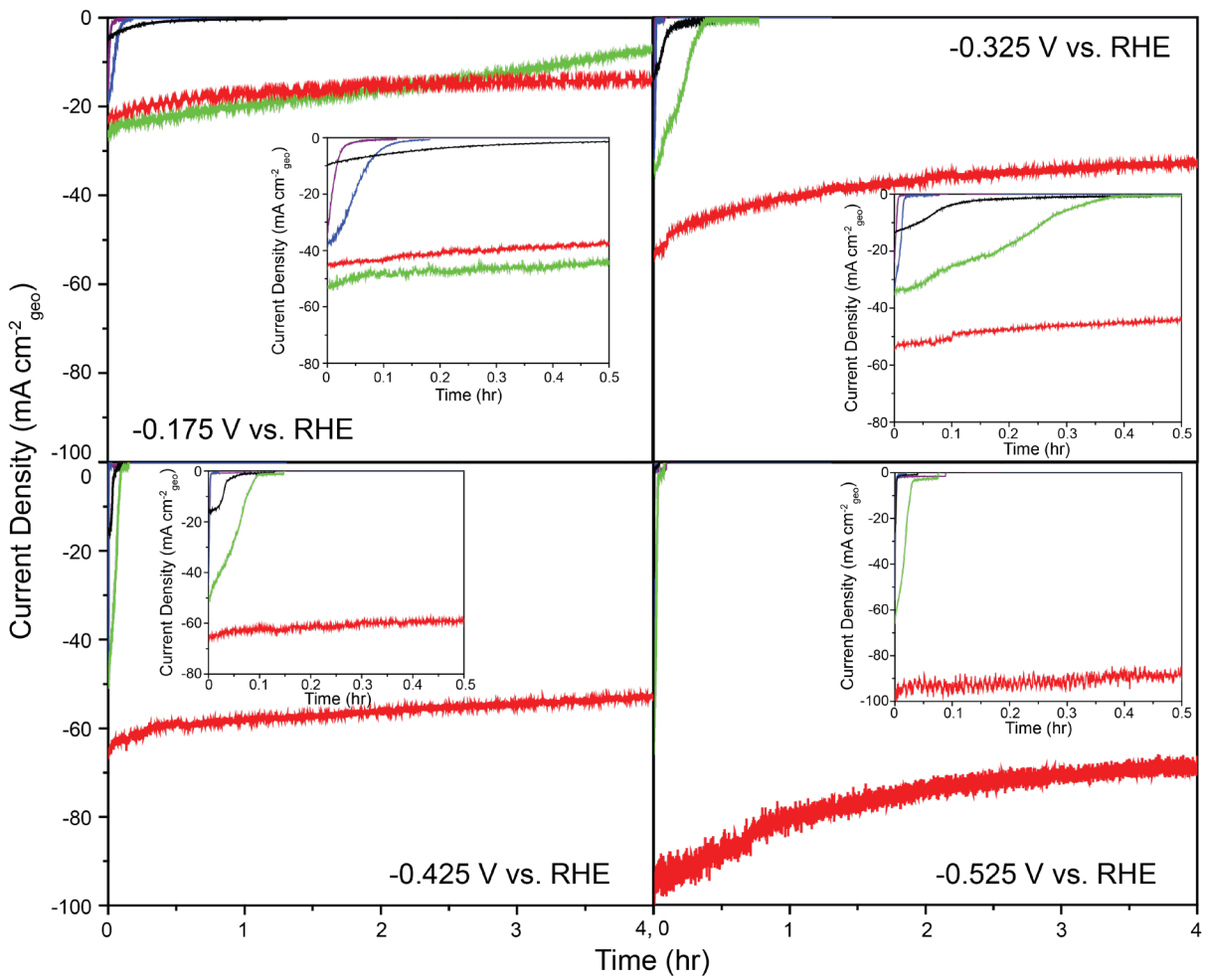


Figure 8: Time transients for CO_2RR electrolysis on np-PdX (X = Co (red), Ni (green), Cu (blue), and Ag (purple)) and Pd/C (black) in CO_2 saturated 1 M KHCO3 at indicated CO_2RR potentials. **Insets:** Early electrolysis time transients to show fast deactivation of all electrodes other than np-PdCo.

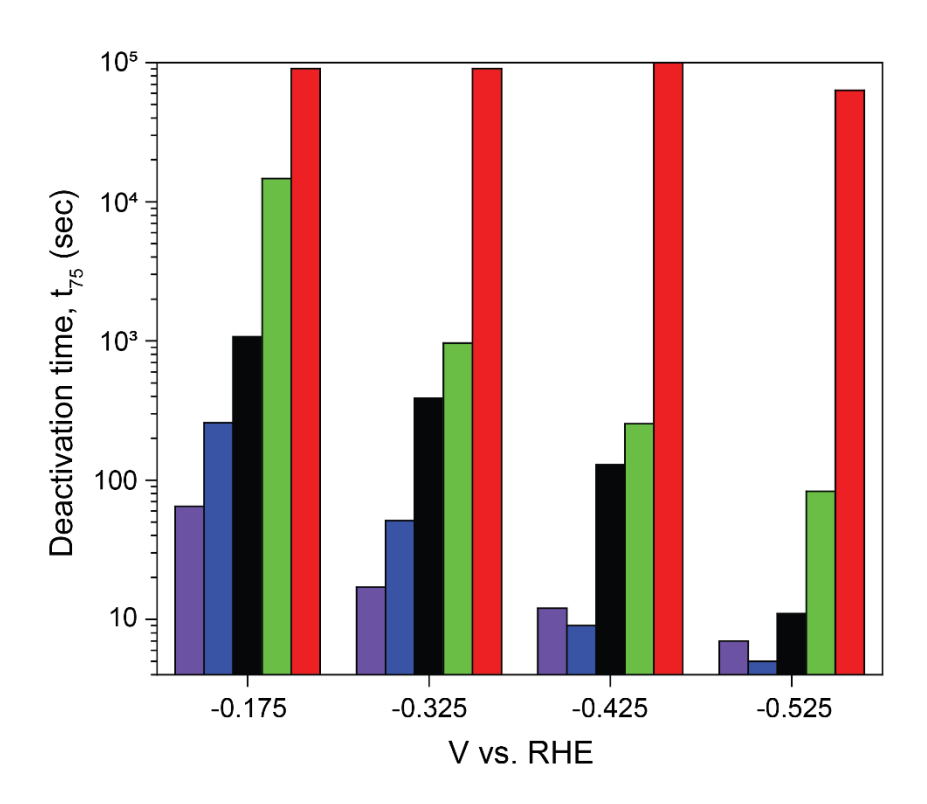


Figure 9: Deactivation time, t₇₅, during constant potential CO₂RR electrolysis in 1 M KHCO₃. t₇₅ is the time required for the electrolysis current to decrease by 75 % from the original value upon initial application of potential. np-PdAg (purple), np-PdCu (blue), Pd/C (black), np-PdNi (green), np-PdCo (red).

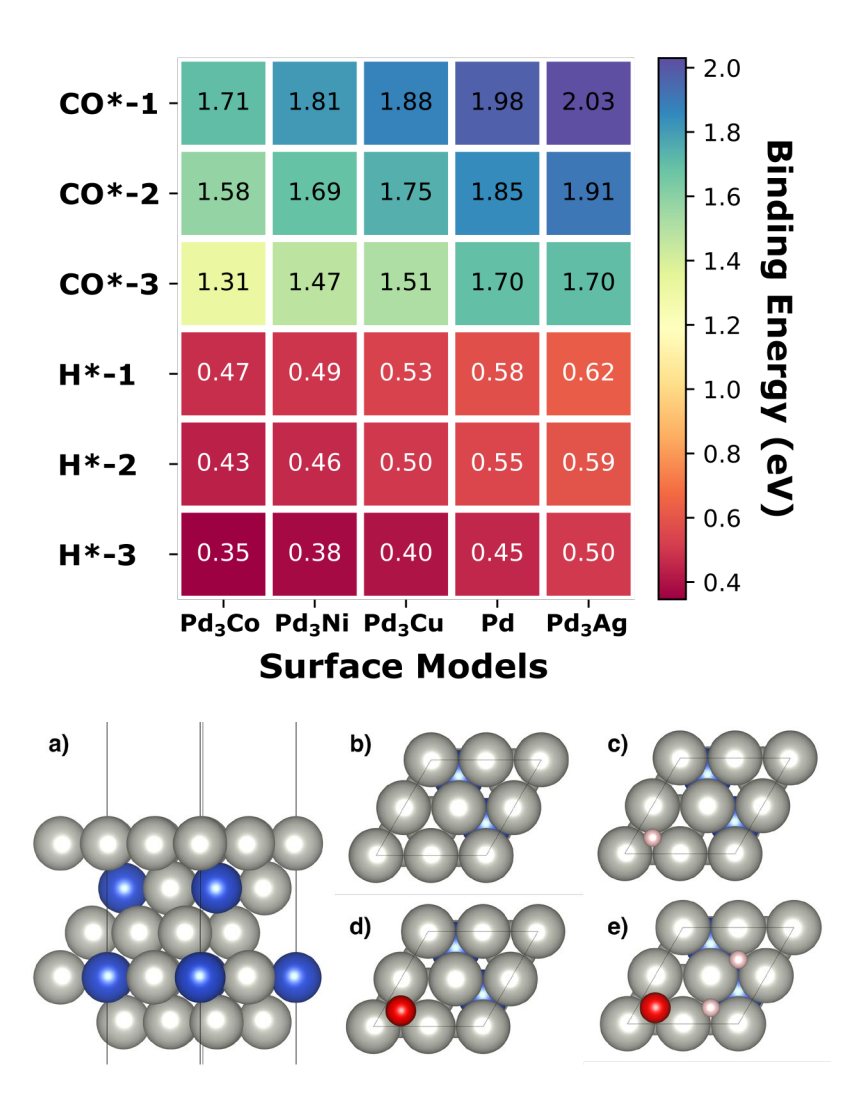


Figure 10: (Top) Tabulated binding energies (in eV) for CO binding to a clean surface (CO*-1), CO binding to a surface with H* (CO*-2), CO binding to a surface with 2 H* (CO*-3), H binding to a clean surface (H*-1), H binding to a surface with H* (H*-2), and H binding to a surface with CO* (H*-3). (Bottom) Representative slab model for Pd-skinned Pd₃X alloys used for calculations. a) Side view of a clean Pd₃X alloy surface, b) top view of a clean Pd₃X alloy surface, c) top view of a Pd₃X alloy surface with CO*, e) top view of a Pd₃X alloy surface with CO*, e) top view of a Pd₃X alloy surface with CO*, e) top view of a Pd₃X alloy surface with CO*.

TOC Graphic

